




Parametric Shape Optimization for Combined Additive–Subtractive Manufacturing

LORENZO TAMELLINI ^{1,7}, MICHELE CHIUMENTI,²
CHRISTIAN ALTENHOFEN,^{3,4} MARCO ATTENE,⁵
OLIVER BARROWCLOUGH,⁶ MARCO LIVESU,⁵ FEDERICO MARINI,¹
MASSIMILIANO MARTINELLI,¹ and VIBEKE SKYTT⁶

1.—Consiglio Nazionale Delle Ricerche, Istituto di Matematica Applicata e Tecnologie Informatiche (CNR-IMATI), Pavia, Italy. 2.—International Center for Numerical Methods in Engineering (CIMNE), Universidad Politècnica de Catalunya, Barcelona, Spain. 3.—Fraunhofer Institute for Computer Graphics Research IGD, Interactive Engineering Technologies, Darmstadt, Germany. 4.—Interactive Graphics Systems Group, Technische Universität Darmstadt, Darmstadt, Germany. 5.—Consiglio Nazionale Delle Ricerche, Istituto di Matematica Applicata e Tecnologie Informatiche (CNR-IMATI), Genova, Italy. 6.—SINTEF Digital, Mathematics and Cybernetics, Oslo, Norway. 7.—e-mail: tamellini@imati.cnr.it

In industrial practice, additive manufacturing (AM) processes are often followed by post-processing operations such as heat treatment, subtractive machining, milling, etc., to achieve the desired surface quality and dimensional accuracy. Hence, a given part must be 3D-printed with extra material to enable this finishing phase. This combined additive/subtractive technique can be optimized to reduce manufacturing costs by saving printing time and reducing material and energy usage. In this work, a numerical methodology based on parametric shape optimization is proposed for optimizing the thickness of the extra material, allowing for minimal machining operations while ensuring the finishing requirements. Moreover, the proposed approach is complemented by a novel algorithm for generating inner structures to reduce the part distortion and its weight. The computational effort induced by classical constrained optimization methods is alleviated by replacing both the objective and constraint functions by their sparse grid surrogates. Numerical results showcase the effectiveness of the proposed approach.

INTRODUCTION

The work described in this article has been developed as part of the Horizon 2020 research and innovation project CAXMan (*Computer Aided technologies for Additive Manufacturing*, see <http://www.caxman.eu>). The objectives of this project were to establish cloud-based toolboxes, workflows as well as a one-stop shop for CAX technologies supporting design, simulation and process planning for additive manufacturing. The project originates from the observation that, due to the constant growth of the additive manufacturing (AM) market, there is an increasing demand for a software ecosystem that enables computer-aided technologies (CAX) support of AM processes and machines from design to production. Thus, the project established novel cloud-based workflows and services for

discrete manufacturing (combinations of additive and subtractive) by addressing simulation-based design and simulation of process planning. One of these workflows is the shape optimization procedure detailed in this article.

Indeed, one of the major reasons for the success of AM is because it enables the fabrication of very complex geometries out of reach with standard manufacturing processes, such as forging, machining or casting. However, the surface quality of AM parts is often not sufficient for industrial applications because of surface roughness and thermal distortions induced by the process. To enhance AM quality and to achieve the required dimensional accuracy, a possible solution consists of adding some extra material (*geometric offset*) to enable the part to be finished by subtractive manufacturing (machining). This solution introduces two limitations:

on the one hand, if too little extra material is added, the surface roughness cannot be removed adequately; on the other hand, adding too much material unnecessarily increases printing time and manufacturing costs. Note that the original dimensions of the *nominal* geometry are compromised by the distortions accumulated during the AM process because of the thermal stresses. Hence, the input for the 3D printer is not the nominal geometry but the so-called *stock* geometry instead. In addition to the geometric offset, we also consider the possibility to add inner cavities to the stock part for saving weight and production time/costs. The generation of inner structures also affects the structural behavior of the entire part, not only regarding the in-service requirements, but also during the manufacturing phases. In fact, reducing the amount of material to be printed as well as increasing the external surface area modifies the thermal behavior in terms of heat accumulation and heat extraction.

Therefore, the main objective of the proposed workflow is the definition of a numerical procedure for the optimization of the stock part design to be provided as input to a metal 3D printer, taking into account the thermal deformation induced by the AM process itself and the following post-production by subtractive machining. The problem is defined as a multi-dimensional constrained optimization analysis, solved using optimization methods (e.g., Refs. 1, 2, and 3). In the literature, few works are available on printer-aware optimization;^{4–8} this is therefore one of the major contributions of this work.

The optimization strategy requires the numerical simulation of the AM process for a number of different stock part designs. This kind of analysis computes the residual stresses and distortions induced by the thermal deformations due to the AM process including the final cooling phase and, eventually, the post-treatment processes.⁹ These computations are very CPU time demanding and require a software platform based on massive parallel computing via sub-domain decomposition methods, octree-based meshing tools and embedded technologies.¹⁰ Hence, to alleviate this inconvenience, a surrogate model for both the objective and constraint functions is adopted to deal with the optimization problem; specifically, a sparse grid method has been adopted in this work.^{11,12}

Moreover, the optimization methodology is implemented in a cloud-based environment that includes different pieces of software (provided by different institutions involved in the project) needed for the definition of the stock-part geometry (STEP format), generation of the inner structure, simulation of the AM process and the outer optimization loop. The implementation allows for an automatic pipeline reducing the CAx service to a user-friendly black-box tool.

The content of this article is organized as follows. “[Methodology](#)” section discusses the overall methodology by focusing on a specific test case (the

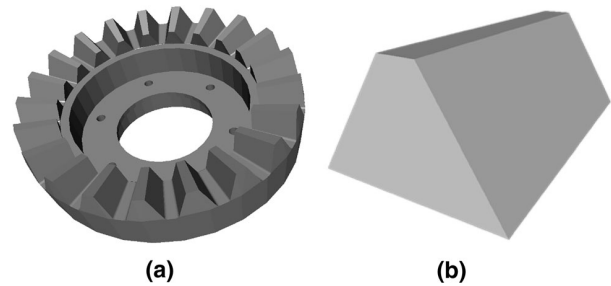


Fig. 1. Gear model provided by STAM (panel a) and a single tooth representing the “nominal geometry” selected (panel b).

generalization to more complex use cases is straightforward). This includes discussion of the specifications of the test case (“[The Industrial Use Case](#)” section), the optimization methodology and the corresponding numerical techniques used for its resolution (“[The Constrained Optimization Method](#)” section), the definition of the surrogate model (“[Surrogate Model Construction](#)” section) and the different steps for the evaluation of the objective and constraint functions according to the stock design parametrization (“[Evaluation of Objective and Constraint Function](#)” section). Some implementation details are given in “[Implementation Details](#)” section. “[Numerical Results](#)” section presents some numerical examples to demonstrate the performance of the optimization algorithm. Finally, “[Conclusions](#)” section summarizes the work, presenting some new perspectives and possible directions for future work. We also refer to the arXiv Ref. 13 which contains a slightly longer version of this manuscript with some additional details.

METHODOLOGY

The Industrial Use Case

The mock-up demonstrator considered in this work is a gear, selected within the CAxMan project and provided by the high-tech engineering company STAM (<http://www.stamtech.com>). Figure 1a shows the nominal geometry of the gear. For the sake of simplification, a single gear tooth (Fig. 1b) as extracted by the original geometry is used to show the optimization strategy proposed in this work. The extension to the entire gear is straightforward.

The Constrained Optimization Method

The final goal is the design optimization of the stock-part geometry to minimize the subtractive (machining) work after the AM stage. The proposed mock-up is parametrized by three parameters: the first one is the offset thickness while the other two parameters are used to control the generation of inner structures as described in “[Generation of Inner Cavities](#)” section. These parameters are collected in the vector $\mathbf{p} \in \Gamma \subset \mathbb{R}^3$. The goal is finding the design variables that minimize the offset thickness allowing for the surface finishing and taking

into account the distortions induced by the AM process and the post-processing operations.

Mathematically, this writes as:

$$\mathbf{p} = \arg \min_{\mathbf{p} \in \Gamma} f(\mathbf{p}) \quad (1)$$

$$\text{st. } g(\mathbf{p}) > 0.04 \text{ mm} \quad (2)$$

$$\Gamma = [p_{1,\min}, p_{1,\max}] \times [p_{2,\min}, p_{2,\max}] \times [p_{3,\min}, p_{3,\max}] \quad (3)$$

where $f(\mathbf{p}) = \Delta \text{Volume}(\mathbf{p})$ is the volume of the extra material, computed as the difference between the volumes of the nominal and the stock geometries, and $g(\mathbf{p}) = \Delta \text{Thickness}(\mathbf{p})$ is the thickness of the material that must be removed from each surface after the 3D printing. Because of the machining tolerance, this thickness must be > 0.04 mm. The Cartesian product $\Gamma = [p_{1,\min}, p_{1,\max}] \times [p_{2,\min}, p_{2,\max}] \times [p_{3,\min}, p_{3,\max}]$ defines the range of variability of the three parameters: the so-called *constraints box*.

Remark 1 The proposed problem can be easily generalized by assuming a different offset thickness and machining tolerance for each one of the surfaces of the geometry.

In this work, the penalization method¹ is used to transform the initial constrained problem into the following modified unconstrained one:

$$\mathbf{p}^* = \arg \min_{\mathbf{p} \in \mathbb{R}^N} f(\mathbf{p}) + \tilde{g}(\mathbf{p}), \quad \mathbf{p} \in \mathbb{R}^N \quad (4)$$

where $\tilde{g}(\mathbf{p}) \gg 0$ if $g(\mathbf{p}) > 0$ to avoid unfeasible solutions. Several methods to build the function $\tilde{g}(\mathbf{p})$ and to solve the unconstrained optimization problem are available in the literature. Because the optimization method requires multiple runs of the AM solver to estimate the distortion of the stock geometry, in this work, functions $f(\mathbf{p}), g(\mathbf{p}), \tilde{g}(\mathbf{p})$ are replaced by surrogate models (approximations) denoted by $F(\mathbf{p}), G(\mathbf{p}), \tilde{G}(\mathbf{p})$. These models are built beforehand by employing a handful of full evaluations of $f(\mathbf{p}), g(\mathbf{p}), \tilde{g}(\mathbf{p})$ only, so that most of the CPU time required to build the surrogate model is spent offline. Given this, the optimization problem is rewritten as:

$$\mathbf{p}^* = \arg \min_{\mathbf{p} \in \mathbb{R}^N} F(\mathbf{p}) + \tilde{G}(\mathbf{p}), \quad \mathbf{p} \in \mathbb{R}^N. \quad (5)$$

In this work, three penalization methods (squared penalty, augmented Lagrangian and log-barrier methods) and two unconstrained optimization techniques for each penalization method (gradient descent and the Nelder–Mead) are investigated to find the best solution for the proposed AM problem. On the one hand, the gradient descent method is very fast, but it might fail if the optimal point is close to

the boundary of the constraint box. On the other hand, the Nelder–Mead technique is slower but generally more robust.

Finally, different initial conditions chosen according to the random Latin hypercube sampling method have been considered to reduce the risk of stagnation in local minima.¹⁴

Surrogate Model Construction

A vast body of literature on surrogate model construction is available: e.g., radial basis functions, reduced basis, proper orthogonal decomposition, neural networks and sparse grids can be used for this scope (see, e.g., Refs. 15, 16, and 17). In this work, the sparse grid method^{11,12} is chosen. This method is suitable to approximate multivariate functions depending on a moderate number of inputs (say, up to a dozen) and has been successfully employed as a surrogate model in optimization problems; see, e.g. Ref. 18. It is easy to use, since it only requires evaluating the functions at hand at some prescribed points, and works well if the function to be approximated is smooth. An example of a set of evaluation points over a three-dimensional constraint box Γ is shown in Fig. 6 in the “Numerical Results” section; each dot represents a set of parameters \mathbf{p} to evaluate $f(\mathbf{p})$ and $g(\mathbf{p})$ and, finally, to build the surrogate models $F(\mathbf{p}), G(\mathbf{p})$ and $\tilde{G}(\mathbf{p})$.

The accuracy of the surrogate model depends on the number of points in the sparse grids. The user chooses the number of points indirectly by setting the integer number w , which represents the “refinement level” of the sparse grid. For instance, the number of points in a sparse grid over a two-dimensional constraint box grows as 1, 5, 17, 49, 129 for $w = 1, 2, 3, 4, 5$. For a three-dimensional constraint box, one would get 1, 7, 31, 111, 351 points for the same values of w .

Given this, the optimization procedure proceeds as follows:

1. Fix the starting sparse grid refinement level w to determine the sparse grid points;
2. For each point (i.e., upon fixing the stock design), evaluate the constraint and objective functions;
3. Build the sparse grid surrogate model by computing the corresponding surrogate constraint and objective functions;
4. Solve the constrained optimization problem (5) obtained by replacing the constraint and objective problem with their sparse grid surrogates;
5. If the result is not satisfactory, increase the sparse grid level w and repeat from point 2.

Remark 2 All the computations required in point 2 can be performed in parallel as they are independent from each other.

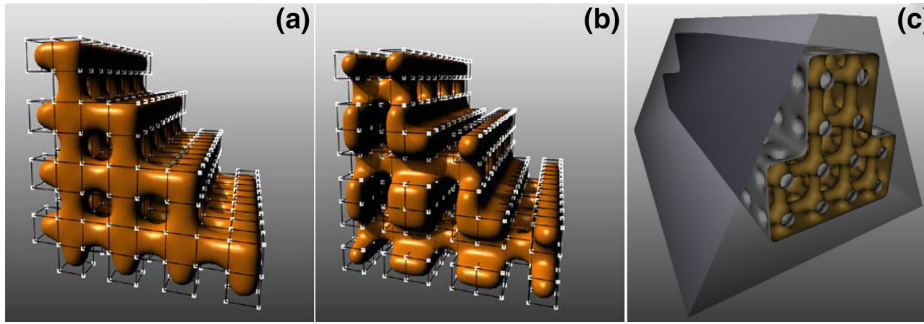


Fig. 2. Three different possible patterns for internal cavities: “tri” (panel a); “H” (panel b); “cross” (panel c). The picture in panel c shows the internal structures inserted in the nominal geometry.

Remark 3 By increasing the sparse grid level w , one generates a new grid that typically includes the previous one, so that all computations already performed can be recycled.

Evaluation of Objective and Constraint Function

Evaluating the objective and constraint function for a given stock design is a complex, multi-stage operation that requires the use of different software. Upon fixing the values of the design parameters \mathbf{p} for the stock design, the following steps are needed:

1. Generation of inner cavities in the nominal geometry;
2. Construction of the stock geometry by offsetting the surfaces of the nominal geometry with the inner cavities;
3. Mesh generation;
4. Simulation of the AM process;
5. Computation of the constraint function $g(\mathbf{p})$ as the distance function between the deformed stock geometry (after manufacturing) and the nominal geometry.
6. Computation of the objective function $f(\mathbf{p})$ as the difference between the volumes of the stock and the nominal geometry, respectively.

Generation of Inner Cavities

To reduce the distortion during the printing process, internal cavities inside the nominal geometry can be generated. In fact, reducing the volume of the part mitigates its thermal deformation. Moreover, introducing such cavities leads to a weight reduction that saves material and printing time. One hypothesis made in this work assumes that the generation of inner cavities is compatible with structural/mechanical performance of the component to be printed. If this is not the case, it is always possible to increase the complexity of the optimization problem adding any mechanical constraint.

Internal cavities are created by fitting a repetitive pattern based on a regular hexahedral grid inside the bounding box of the nominal geometry. Different patterns hold different thermo/mechanical

behaviors in terms of heat diffusion, structural stiffness and material savings. The intersection (Boolean operation) between the volume of the nominal geometry and the structure chosen for the inner cavities leads to the final geometry of the component.

The geometries of the inner structures are based on Catmull–Clark (CC) subdivision surfaces.¹⁹ This technique is commonly used in computer graphics and animation and is increasingly used in the engineering sector. CC subdivision allows for defining smooth surfaces (C^2 -continuous in regular areas, C^1 -continuous around extraordinary points) based on a discrete control mesh. Regular CC subdivisions correspond to bi-cubic B-spline surfaces, and therefore the geometry of the internal structures can be converted into a CAD-compatible representation.

Figure 2 shows three possible patterns repeated in a grid-based manner. By alternating different patterns, it is possible to treat different regions of the part according to local structural requirements. Note that 90° angles between grid cells result in a curved geometry due to the smoothing property of CC surfaces. This is beneficial in terms of manufacturability because modern AM machines (especially SLS and SLM machines) are able to manufacture overhangs of up to 45° , unless the geometry has a curved, arch-like shape. Therefore, the overall quality of the inner cavities is quite good in terms of surface quality and dimensional control. In this work, the so-called “cross” pattern is adopted as shown in panel c of Fig. 2. The generation depends on two parameters: the grid resolution (size of the cavities) and the minimum wall thickness between the cavities and the outer surface of the object. Both parameters belong to the optimization space Γ .

Geometry Offset and Mesh Generation

In this work, starting with an initial tessellated geometry, the objective is to obtain an “inflated” geometry (offset) satisfying the required allowance. Unfortunately, a plain offsetting cannot be used because the class of polyhedra is not closed under the offsetting operation. Therefore, exact offsetting

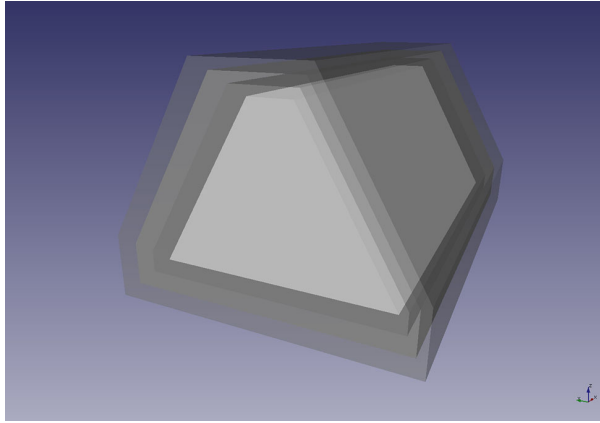


Fig. 3. Nominal geometry with different offset radii.

might be possible for a very small set of simple geometries, only.

An offset can be seen as a particular case of a so-called *Minkowski sum*. Hence, denoting a solid object by M (e.g., a sphere), then an arbitrary Minkowski sum can be used to get the offsetting by rolling M over the surface S of the nominal geometry. The result is denoted by $S \oplus M$. Thus, if M is a sphere with radius r , the Minkowski sum $S \oplus M$ is equal to $\text{Offset}_r(S)$. Note that the Minkowski sum of two polyhedra is a polyhedron. Thus, we exploited this result to implement an approximated offsetting whose result is a polyhedron with guaranteed distance bounds from S . Our implementation uses the CGAL library²⁰ and the concept of the NEF polyhedron.²¹ In the experiments reported in this article, the solid M used to obtain the Minkowski sum is a cube. Figure 3 shows the nominal geometry of the tooth as it is used in the optimization process, together with offset geometries of different radii.

Merging the data structures of the offset nominal geometry and the internal cavities allows for representing the complete (tessellated) boundaries of the simulation domain. Starting from this file, an appropriate tetrahedral mesh of the domain can be created with the aid of the CGAL library and its 3D meshing functionalities.²² This tetrahedral mesh is then passed forward to the subsequent stage where the simulation of the printing process is performed.

Printing Process Simulation

The EOS M280 is the selective laser melting (SLM) printer considered in this work. The printing process consists of uniformly spreading the loose powder by a wiper to form a new layer ready for the laser melting. A user-defined scanning sequence drives the heat source (laser) to selectively melt this new layer according to the geometry of the component. The process is repeated until the stock part is built.

From the computational point of view, different approaches have been developed for the numerical simulation of this process. The most accurate one

requires the solution of the fully coupled thermo-mechanical problem together with a high-fidelity representation of the scanning path.^{9,23} These approaches provide a reliable and accurate prediction of the distortion and residual stresses but are expensive in terms of computational resources and CPU time. Nowadays, the numerical simulation of large industrial components is still unfeasible with standard computers, and the use of massive parallel computing in distributed memory is mandatory.^{10,24} Consequently, the implementation of a simplified method is necessary to reduce the CPU time. In this work, the *inherent strain method* is adopted.^{10,24,25}

The main hypothesis allowing for the use of the inherent strain method assumes a localized heat source so that the heat-affected zone (HAZ) is very small, not affecting the rest of the domain. Given this, the classical coupled non-linear thermo-mechanical analysis is replaced by a sequence of mechanical computations according to the layer-by-layer deposition strategy. The inherent strains are defined as the sum of both the thermal and the plastic strains induced by the manufacturing process. More precisely the thermal shrinkage of each new layer is estimated (offline) according to the melt-pool temperature and the thermal expansion coefficient, while the plastic strains are calibrated according to the scanning speed and the power heat.²⁵ Hence, all the elements belonging to a new layer are *activated* to form part of the current computational domain. For each new layer, the corresponding thermo-mechanical loading is given in terms of inherent strains at each Gaussian quadrature point.

The computation is performed assuming a layer-by-layer deposition by skipping the high-fidelity simulation of the scanning sequence necessary to complete each layer of the domain. Nonetheless, still a huge number of layers (corresponding to an equal number of simulation steps) is necessary to deal with the numerical simulation. As a result, an extremely fine mesh (smaller than the layer thickness of about 20–30 μm thick) is also required, increasing the CPU time per simulation. However, through sensitivity analysis a multi-layer activation process has been investigated, showing that it is possible to pack up to ten layers per single activation without losing the original accuracy. Hence, up to 200 μm can be used as a reference thickness for the layer-by-layer analysis. The simulation time can be accelerated by a factor of 10 allowing the AM simulation kernel to be part of the optimization loop.

The other important hypotheses of the numerical simulation strategy are the following: First, the back plate is generally not analyzed. Instead, the corresponding clamping conditions are taken into account by means of full displacement prescriptions at the contact surface between the part and the back plate. Second, the loose powder has been virtualized; thus, it is neither discretized nor computed.

This is due to the fact that, from the thermal point of view, the powder can be tackled as almost adiabatic boundary conditions, while mechanically, its stiffness is negligible if compared with the bulk (sintered material). Finally, the effects induced by the supporting structures have been accounted for. Their geometrical description as well their discretization by the FE mesh has been avoided to reduce the computational time while preserving the accuracy of the results. Instead, an equivalent stiffness has been computed and assembled into the global system of equations at each node connecting the part to the back plate. This equivalent stiffness takes into account both the length and the effective area of each supporting structure as well as the fact that they are built by sintering the same powder as for the component. Hence, the Young's modulus of the supporting structure is the same as for the AM part under construction.

The final result coming from the manufacturing process simulation is presented in terms of accumulated distortions of the component according to the AM sequence. Those deformations will define a distorted volume of the stock geometry to be compared with the nominal one. Comparisons with both the experimental evidence through the 3D printing of ad hoc samples or by analyzing the results obtained by high-fidelity fully coupled thermo-mechanical analysis have been carried out.²⁵

The proposed AM model has been implemented into the software package COMET,²⁶ a finite element-based platform for the analysis of coupled thermo-mechanical problems. Pre- and post-processing is done with the GiD software,²⁷ developed at CIMNE, the International Center for Numerical Methods in Engineering.

Computation of the Objective and Constraint Functions

The objective function requires the evaluation of the volume of the extra material to be removed from the stock part by machining. This volume can be obtained by subtracting the volume of the nominal geometry (including the internal cavities) from the volume of the printed stock part obtained after the AM process simulation by summing the volumes of all the tetrahedra of the deformed mesh. Hence:

$$\Delta\text{Volume} = \text{Distorted mesh volume} - (\text{Nominal geometry} - \text{Internal cavities}). \quad (6)$$

To evaluate the constraint function of the optimization problem, it is necessary to compute the distance between the nominal and the stock geometry at each of the points belonging to the tessellation of the external surfaces. The method consists of an iterative solution to find the orthogonal projection of each point to the (smooth) surface defining the nominal geometry. This computation is based on an

iterative closest point projection method.²⁸ If the closest point projection results in a point outside the domain, then the distance is computed with respect to the closest boundary of the trimmed surface.

Implementation Details

One objective of the CAxMan project was the automatic interoperability among the different pieces of software required by the AM optimization methodology through a cloud-based system. This complex workflow is enhanced by designing suitable API and favoring standard formats like STEP. Docker containers have been used to simplify the deployment of each piece of software.²⁹ More in detail, the software used is the following: SG++^{18,30} to generate the sparse grids and to solve the optimization problem; in-house software to generate the internal cavities; CGAL routines³¹ for the geometry offset and the mesh generation; COMET²⁶ for the simulation the AM process and to compute the volume of the stock-part after 3D printing; GiD²⁷ for the result post-processing; GoTools³² to compute the distances between the distorted stock-part and nominal geometry. Figure 4 shows the flowchart of the implemented optimization methodology.

NUMERICAL RESULTS

The results of the optimization methodology presented are discussed here. A sequence of tests of increasing complexity is considered by extending the number of optimization parameters. Ti64 is the reference powder material used for the printing process, and the following properties are required for the AM process simulation. The density of the material is 4420 kg/m³, the Young modulus is 1.18e+11 Pa, and the Poisson ratio is 0.33. The thermal expansion coefficient is 9e−06, the metal deposition temperature is 700°C, and the annealing temperature is 800°C. The elastic limit is 954e+06 Pa, and the ultimate stress is 1110e+06 Pa. Finally, the nominal geometry is contained in a bounding box of 10 mm × 6 mm × 4 mm, and the machining tolerance is set as 0.04 mm.

Optimization of the Offset Thickness

This analysis focuses on the optimization of the offset thickness only. The offset value ranges between 0 and 1 mm. The AM simulation uses a mesh defined by approximately 500 K tetrahedra. The optimization workflow is performed four times by increasing the sparse grid level from $w = 2$ to $w = 5$, until reaching the required accuracy (i.e., the optimal thickness value computed for $w = 4$ and $w = 5$ varies less than 1e−4 mm).

Figure 5 shows the surrogate models ($w = 4$) of the objective (panel a) and constraint functions (panel b), respectively. The constraint function is actually rewritten as $0.04 \text{ mm} - \Delta\text{Thickness}(p) < 0$

Parametric Shape Optimization for Combined Additive–Subtractive Manufacturing

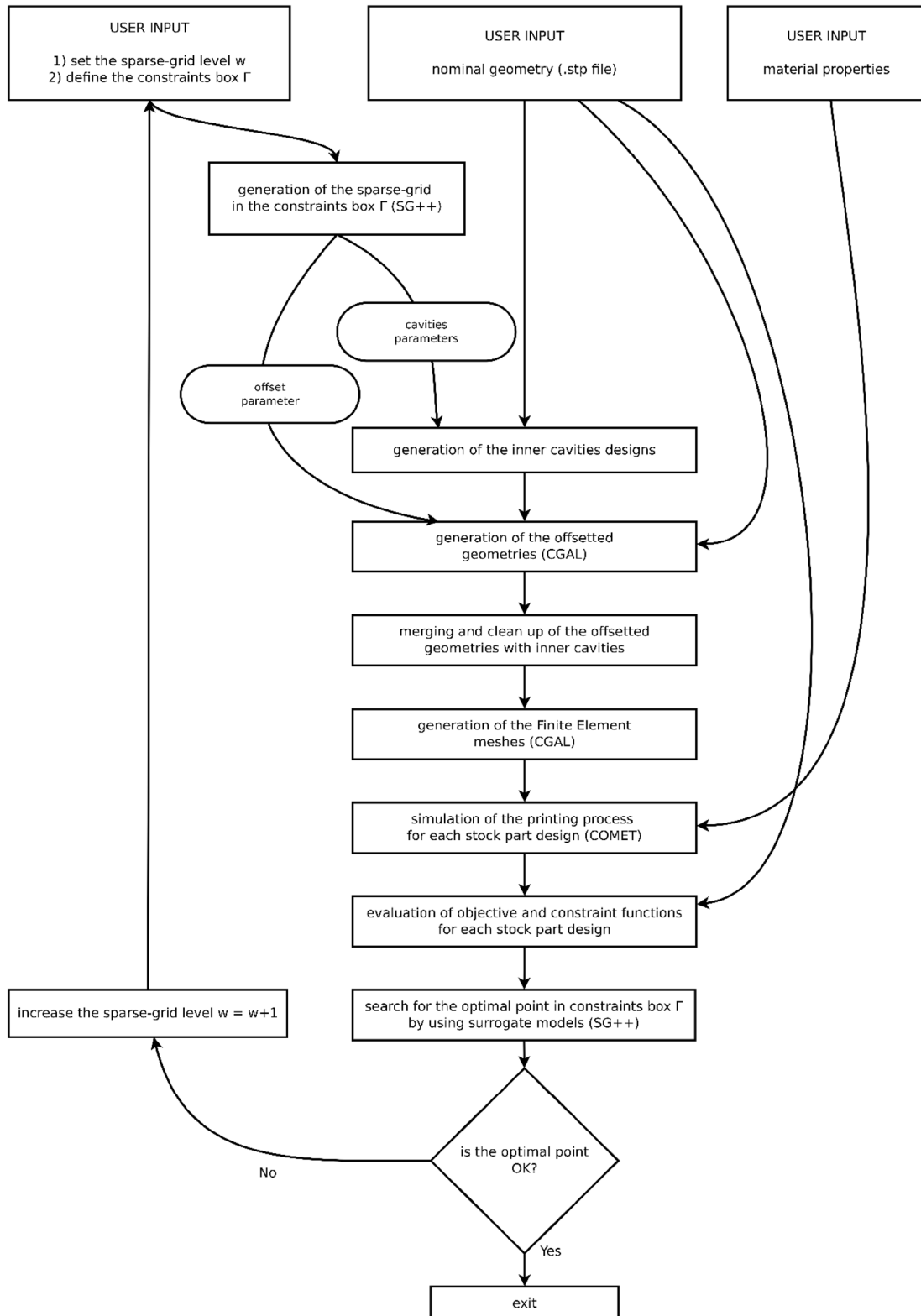


Fig. 4. Software flowchart for the optimization methodology implemented.

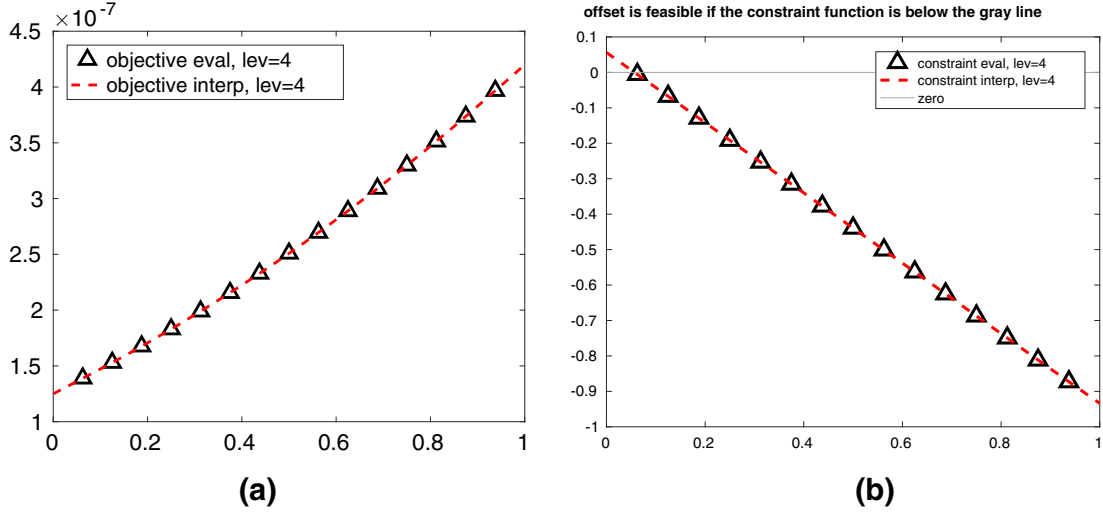


Fig. 5. Surrogate model for objective (panel a) and constraint (panel b) functions for $w = 4$ when optimizing the offset radius. The plot of the constraint function also shows the feasible region, where the original constraint function is positive.

Table I. Results of the optimization test to find the optimal offset radius

w	Design points	Optimal offset (mm)	Optimal volume (mm ³)	Best method	Interpolant evaluations	Computational time (hh:mm:ss)
2	3	0.0569	132.67	Squared penalty with gradient	52	00:12:01
3	7	0.0571	136.93	Squared penalty with gradient	50	00:25:41
4	15	0.0567	137.59	Squared penalty with gradient	49	00:56:35
5	31	0.0567	137.62	Squared penalty with gradient	48	01:57:14

because of the requirements of the optimization software. The black triangles represent the values computed by the evaluation of the full model (i.e., performing all the steps described in “[Evaluation of Objective and Constraint Function](#)” section), while the red dotted lines represent the surrogate functions computed offline. As expected, the objective function (i.e., the volume) increases as the offset thickness increases, faster than linearly. The distance between the nominal and the distorted surfaces also becomes larger and larger as the offset increases. Hence, the constraint function becomes increasingly negative. Note that if the constraint function is positive, the offsetting is not feasible because the machining tolerance is not satisfied.

The results obtained through the optimization methodology are reported in Table I. The column “interpolant evaluations” in Table I reports the total number of evaluations required by the surrogate models of the objective and the constraint functions performed to compute the optimal design point. These values would roughly correspond to the number of solutions required by the optimization

process when the sparse grid surrogate model is not used. The value is much larger than the number of design points, meaning that significant computational time is saved with the proposed procedure. In this work, the optimization procedure was repeated according to the six variants of the method and for five starting points to find the exact optimal value of the offset. The column “method” shows the best penalization method (squared penalty, augmented Lagrangian, log-barrier) and the unconstrained optimizer used (gradient, Nelder–Mead).

Optimization of Offset Thickness and Cavity Parameters

The next optimization analysis that we report is the joint optimization of the offset thickness and both parameters needed by the cavity generation algorithm. We refer to Ref. 13 for additional optimization analyses where only two parameters are considered (the offset thickness and only one parameter for the cavity generation). Sparse grids of level $w = 2, 3$ are used because level $w = 4$ would

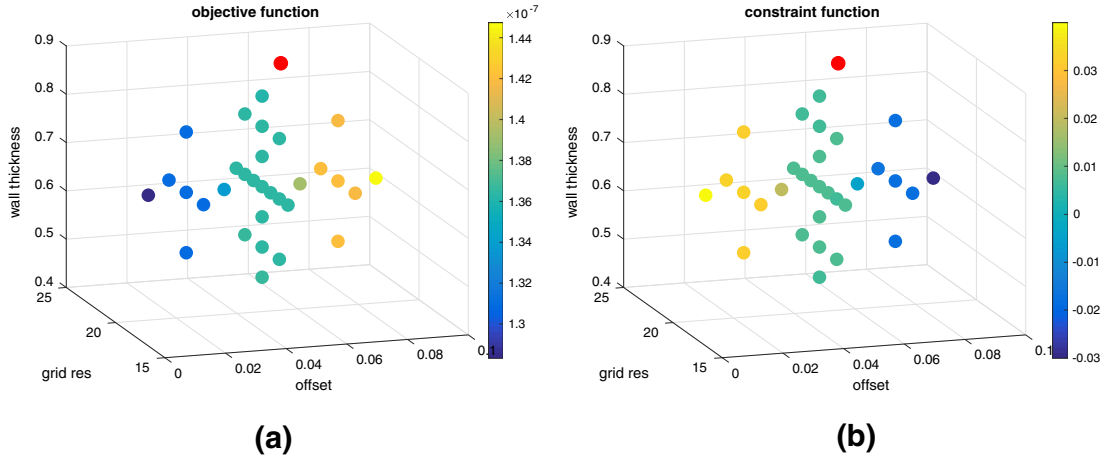


Fig. 6. Plot of objective and constraint functions (panels a and b, respectively) for the optimization over three parameters.

Table II. Optimizing offset radius and both inner cavities generation parameters

w	Design points	Optimal offset (mm)	Optimal volume (mm ³)	Optimal grid resolution	Optimal wall thickness	Method	Interpolant evaluations	Computational time (hh:mm:ss)
2	7	0.0551	137.24	17	0.9	Aug. Lagrangian with Nelder Mead	2008	00:34:35
3	31	0.0566	137.54	20.65	0.9	Squared penalty with Nelder Mead	2057	02:27:23

require an excessive CPU time. The variation ranges of the three parameters are as follows: offset 0–0.1 mm, grid resolution 17–24, wall thickness 0.4–0.9 mm.

The results in this case are reported in Fig. 6 and Table II. Figure 6 shows the three-dimensional constraint box in which the problem is defined. Each dot is a sparse grid point where the full model is evaluated (for the sparse grid at level $w = 3$). In panel a, dots are colored in blue-to-yellow shades according to the value of the objective function, while in panel b the value of the constraint function has been considered. The red dot represents instead the optimal point selected by the optimization algorithm. It can be easily seen that most of the variability is due to the offset parameter for both objective and constraint functions. Specifically, the optimal offset thickness is around 0.056 mm; the values selected for the wall thickness and grid resolution are irrelevant to the optimization and therefore they are not constant across values of w . Finally, observe the much larger number of surrogate model evaluations needed by the Nelder–Mead algorithm for this optimization case. This number is so large that trying to solve the optimization

problem without replacing the full model with its surrogate model approximation would be impossible.

CONCLUSION

The main objective of this work is the definition of the procedure for the optimization of the stock part design to be provided as input to a metal 3D printer, keeping into account the thermal deformation induced by the AM process. The problem is defined as a multi-dimensional constrained optimization analysis, where the constraint and objective functions have been replaced by their sparse grid surrogate models to achieve the best computational efficiency.

The proposed optimization procedure is fully automatic. The workflow makes use of different software modules (most of them in-house solutions) as part of the optimization loop to deal with the CAD geometry, the offsetting procedure, the inner cavities generation and the AM solver, among others. A cloud-based environment together with HPC facilities reduced the computational time while keeping the CAx tool transparent to the AM end-user.

For the proposed demonstrator, up to three different parameters have been optimized: the offset thickness and two parameters related to the inner cavity generation. The optimization of the stock part can be enhanced improving the proposed strategy as follows. First, one could assume different offsets on different region of the geometry. Second, the generation of inner cavities could be subjected to mechanical or thermal constraints. In this case, also the analysis of the mechanical/thermal performance of the component under the actual mechanical/thermal loading for each stock part design would be required as part of the optimization loop. Finally, the post-processing phase also causes a change in the final shape because of the stress release due to the heat treatment or the subtractive operations. Therefore, a numerical framework to simulate the entire manufacturing chain in AM could be used to predict the evolution of the residual stresses and the corresponding part distortion.

ACKNOWLEDGEMENTS

This work was funded by the European Union's Horizon 2020 research and innovation program under Grant Agreement No. 680,448 CAXMan, Computer-Aided technologies for Additive Manufacturing.

REFERENCES

- J. Nocedal and S. Wright, *Numerical Optimization*, 1st ed. (New York: Springer, 1999).
- G. Allaire, F. Jouve, and A. Toader, *J. Comput. Phys.* 194, 363 (2004).
- E. Picelli, S. Townsend, C. Brampton, J. Norato, and A. Kim, *Comput. Methods Appl Mech. Eng.* 329, 1 (2018).
- Y. Wang and Z. Kang, *Comput. Methods Appl Mech. Eng.* 329, 553 (2018).
- C. Dapogny, R. Estevez, A. Faure, and G. Michailidis, *Comput. Methods Appl Mech. Eng.* 344, 626 (2019).
- F. Zwicke, M. Behr, and S. Elgeti, *AIP Conf. Proc.* 1896, 100001 (2017).
- G. Allaire, C. Dapogny, R. Estevez, A. Faure, and G. Michailidis, *J. Comput. Phys.* 351, 295 (2017).
- S. Cacace, E. Cristiani, and L. Rocchi, *Appl. Math. Model.* 44, 446 (2017).
- M. Chiumenti, E. Neiva, E. Salsi, M. Cervera, S. Baida, J. Moya, Z. Chen, C. Lee, and C. Davies, *Addit. Manuf.* 18, 171 (2017).
- E. Neiva, S. Badia, A.F. Martin, and M. Chiumenti, *Int. J. Numer. Methods Eng.* 119, 1098 (2019).
- H.-J. Bungartz and M. Griebel, *Acta Numer.* 13, 147 (2004).
- F. Nobile, L. Tamellini, and R. Tempone, *Numer. Math.* 134, 343 (2016).
- C. Altenhofen, M. Attene, O. Barrowclough, M. Chiumenti, M. Livesu, F. Marini, M. Martinelli, V. Skytt and L. Tamellini, Parametric shape optimization for combined additive-subtractive manufacturing,” (arXiv preprints, 2019). <https://arxiv.org/abs/1907.01370>. Accessed Oct. 2, 2019.
- M. McKay, R. Beckman, and W. Conover, *Technometrics* 21, 239 (1979).
- M. Buhmann, *Radial Basis Functions: Theory and Implementations*, 1st ed. (Cambridge: Cambridge University Press, 2003).
- F. Ballarin, A. Manzoni, A. Quarteroni, and G. Rozza, *Int. J. Numer. Methods Eng.* 102, 1136 (2014).
- C. Higham and D. Higham, Deep Learning: An Introduction for Applied Mathematicians (arXiv preprints, 2018). <https://arxiv.org/abs/1801.05894>. Accessed Oct. 2, 2019.
- J. Valentin and D. Pflüger, Hierarchical Gradient-Based Optimization with B-Splines on Sparse Grids, *Sparse Grids and Applications—Stuttgart 2014*, ed. J. Garcke, D. Pflüger (Springer 2016), p. 315.
- E. Catmull and J. Clark, *Comput. Aided Des.* 10, 350 (1978).
- A. Fabri, M. Teillaud, CGAL, The Computational Geometry Algorithms Library (10ème Colloque National en Calcul des Structures, 2011), <https://hal.archives-ouvertes.fr/CSMA2011/hal-00592685v1>. Accessed Oct. 2, 2019.
- P.K.L. Hachenberger, L. Kettner, and K. Mehlhorn, *Comput. Geom.* 38, 64 (2007).
- R.Y.M. Laurent, *Comput. Geom. Theory Appl.* 38, 100 (2007).
- M. Chiumenti, X. Lin, M. Cervera, W. Lei, Y. Zheng, and W. Huang, *Rapid Prototyp. J.* 23, 448 (2017).
- E. Neiva, M. Chiumenti, M. Cervera, E. Salsi, G. Piscopo, S. Badia, A. Martin, Z. Chen, C. Lee and C. Davies, Numerical modelling of heat transfer and experimental validation in Powder-Bed Fusion with the Virtual Domain Approximation (arXiv preprints, 2018). <https://arxiv.org/abs/1811.12372v4>. Accessed Oct.2, 2019.
- I. Setien, M. Chiumenti, S. van der Veen, M. San Sebastian, F. Garciandía, and A. Echeverría, *Comput. Math. Appl.* 78, 2282 (2019).
- M. Cervera, C. Agelet de Saracibar and M. Chiumenti, COMET: Coupled Mechanical and Thermal Analysis. Data Input Manual, Version 5.0 (CIMNE technical report IT-308, 2002). https://www.cimne.com/comet/cvdata/cntr1/dtos/mdia/COMET_Data_Input_manual.pdf. Accessed Oct. 2, 2019.
- CIMNE, Technical University of Catalonia, GiD: the Personal Pre and Post-Processor (2002). <http://gid.cimne.upc.edu>. Accessed Oct. 2, 2019.
- P.J. Besl and N.D. McKay, *IEEE Trans. Pattern Anal. Mach. Intell.* 14, 239 (1992).
- Docker Inc., Docker. www.docker.com. Accessed Oct. 2, 2019.
- The SG++ Project, SG++ (2008). <http://sgpp.sparsegrids.org>. Accessed Oct. 2, 2019.
- The CGAL Project, CGAL (1995). www.cgal.org. Accessed Oct. 2, 2019.
- SINTEF Digital, GoTools: Geometry Toolkit. <https://github.com/SINTEF-Geometry/GoTools> (2018). Accessed Oct. 2, 2019.

Publisher's Note Springer Nature remains neutral with regard to jurisdictional claims in published maps and institutional affiliations.